

Drift Chamber Alignment using Cosmic Rays

Ashutosh V. Kotwal¹

Duke University

Christopher P. Hays

Oxford University

Abstract

The Collider Detector at Fermilab (CDF) is a general-purpose experimental apparatus with an inner tracking detector for measuring charged particles, surrounded by a calorimeter for measurements of electromagnetic and hadronic showers, and a muon detector system. We present a technique for, and results of, a precise relative alignment of the drift chamber wires of the CDF tracker. This alignment has been an important component of the track momentum calibration, which is the basis for the charged-lepton calibration for the measurement of the W boson mass at CDF.

Key words: drift chamber, alignment, cosmic ray, calibration.

PACS: 06.60.Sx, 06.30.Bp, 07.05.Kf, 07.77.Ka, 07.90.+c, 29.30.Aj, 29.40.-n, 29.40.Gx, 29.40.Cs, 29.90.+r

1 Introduction

The measurement of the W boson mass with the CDF detector [1] at the Fermilab Tevatron $p\bar{p}$ collider achieves a precision of one part per 10,000 on the measured energy of muons from W boson decays [2]. A key component of the momentum calibration is a precise relative alignment of the wires in the CDF drift chamber. In this paper we describe the alignment technique developed at CDF using cosmic rays collected *in situ* with collider operation. This technique was initiated in 2002 and used to perform the alignment for the first two measurements of the W boson mass from the CDF Run II data, based on 200 pb^{-1} [1] and 2.2 fb^{-1} [2] of integrated luminosity, respectively. We also

¹ Corresponding author. Tel: (919) 660-2563; fax: (919) 660-2525; E-mail address: ashutosh.kotwal@duke.edu

present the results from the alignment analysis performed most recently using cosmic rays collected during the entire Run II collider operation, to be used in the next W -boson mass measurement at CDF.

The momentum calibration [2] is performed in two steps. First, the selected cosmic-ray sample is reconstructed using special pattern-recognition and track-fitting algorithms that reconstruct the complete cosmic-ray trajectory through both halves of the drift chamber. These algorithms and their performance are described in [3]. This fitted trajectory proves an excellent reference, with respect to which the average hit residuals can be minimized to achieve an internal alignment of the wires. Certain degrees of freedom associated with deformations of the tracker endplates cannot be constrained by minimizing residuals with respect to collider tracks. Examples of such deformations are relative rotations of the inner and outer cylinders of the drift chamber, and relative twists of the east and west endplates. They result in parameter biases in collider track fits but do not result in displaced residuals. On the other hand, such deformations result in differences between the trajectories on the two sides of the drift chamber of the same cosmic ray, and can be constrained by using the complete two-sided helix fit. This property is exploited to remove a number of important sources of bias in the measurement of collider tracks.

In the second step of the calibration, $J/\psi \rightarrow \mu\mu$ and $\Upsilon \rightarrow \mu\mu$ mass peaks are reconstructed with the above alignment. Using the precisely known masses of these particles, a momentum scale factor and the ionization energy loss model are tuned simultaneously in the simulation, and then applied to the W boson mass measurement [1]. Residual misalignments that cannot be constrained with cosmic-ray tracks are corrected using the ratio of calorimeter energy to track momentum of electrons and positrons from W -boson decays [1,2].

In the following we describe the procedure and the results obtained from the cosmic ray alignment. In Sec. 2 we provide a summary of the CDF drift chamber construction and the degrees of freedom we allow in the alignment procedure. In Sec. 3 we describe the spatial and kinematic distributions of the cosmic ray sample recorded with the CDF detector, and the sample selection. In Sec. 4 we show comparisons of the position residuals before and after the alignment procedure is performed. Corrections to the wire shape due to gravitational sag and electrostatic deflection are discussed in Sec. 5. The tuning of the drift model is discussed in Sec. 6. Finally, in Sec. 7 we show the reduction in the track parameter biases, as determined from the comparison of the two segments of the cosmic ray track.

2 Alignment degrees of freedom

The CDF detector [1,4,5,6] is shown in Fig. 1. The central tracking drift chamber [7] (COT) uses an open-cell geometry with 30,240 sense wires. Its tracking volume extends from an inner radius of 41 cm to an outer radius of 138 cm, with a longitudinal extent of 310 cm. A superconducting solenoid immediately outside the COT provides a nearly uniform 1.4 T magnetic field in the tracking volume. Within the COT sits a silicon detector to provide precise vertexing information. In the measurement of the W -boson mass, the momentum of the charged lepton produced promptly in the collision is measured using COT information and constrained to the beam collision region in the transverse plane; silicon detector hits do not improve the precision on the beam-constrained track parameters and are not used.

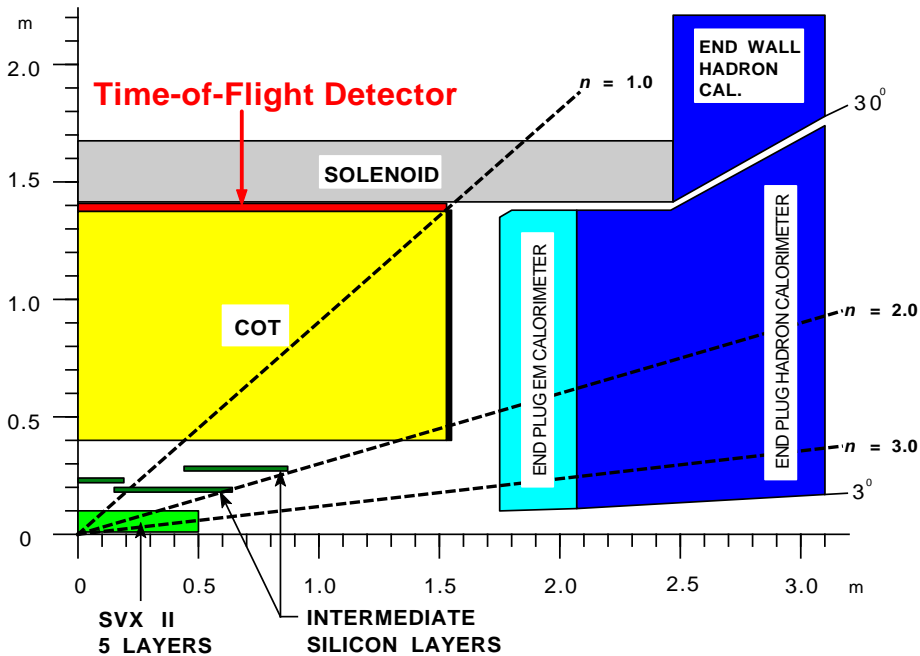


Fig. 1. A cut-away view of the CDF detector, reproduced from [7]. Not shown are the barrel calorimeters outside the solenoid, and the muon detectors outside the calorimeters.

A section of one of the aluminum endplates of the COT is shown in Fig. 2. The drift chamber consists of 2520 drift cells, each containing 12 sense wires. The maximum drift distance is ≈ 8.8 mm. The cells are arranged in 8 radial superlayers (SL0 to SL7), with the number of cells per superlayer increasing with radius. Alternating superlayers consist of wires running along the longitudinal axis (axial superlayers) and wires with a $\pm 2^\circ$ stereo angle (stereo superlayers). The stereo angle changes sign from one stereo superlayer to the

next.

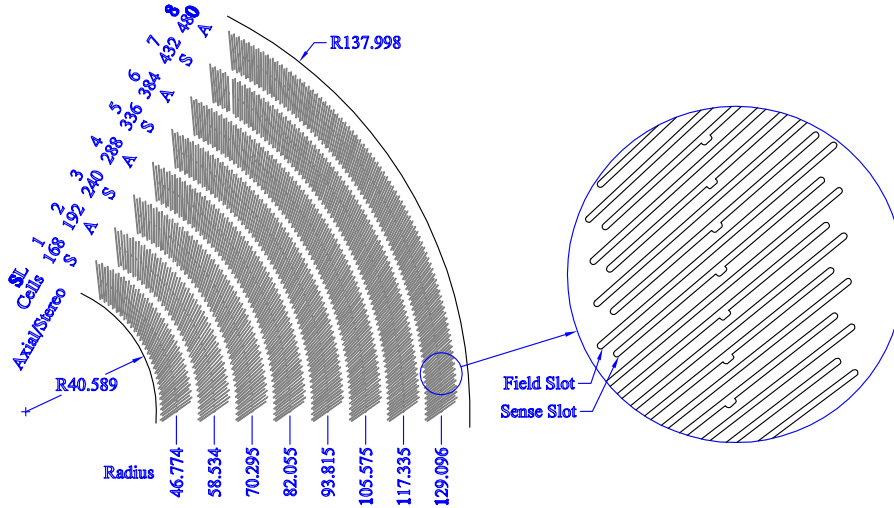


Fig. 2. A section of an aluminum endplate of the COT, reproduced from [7]. The slots cut in the endplates anchor individual drift cells containing 12 sense wires each.

The radial spacing between sense wires in a cell is 5.8 mm [7]. The wires are attached at their ends to rigid cards which are precision-mounted on the COT endplates. In the alignment model, each cell's profile at the endplates is described by a straight line (see Fig. 3). Thus, the degrees of freedom to be constrained in order to precisely locate each sense wire at each endplate are the following:

- (1) the transverse (x, y) coordinates of the center of each cell, at the longitudinal (z) coordinate ± 155 cm of the two endplates.
- (2) the tilt angle (τ) of each cell relative to the radial vector from the transverse origin to the center of the cell at $z = \pm 155$ cm.

We parameterize the former degrees of freedom in terms of symmetrized (i.e. averaged over the two endplates) and anti-symmetrized (i.e. difference between the two endplates) cell-center coordinates. The advantage of these definitions is that the symmetrized and anti-symmetrized cell-coordinate residuals are, to a large extent, uncorrelated because of the approximately uniform and symmetric distribution of the cosmic rays in the z -coordinate. The symmetrized cell-coordinate residuals are averaged over z , while the anti-symmetrized corrections are sensitive to the dependence of the hit residuals on the z -coordinate.

The cell-tilt angle (τ) is designed to account for the Lorentz angle of the drift direction given the magnitude of the electric field, the spectrometer magnetic field and the drift speed. The alignment corrects for small deviations in the cell tilt. The corrections are found to be almost the same for the two endplates.

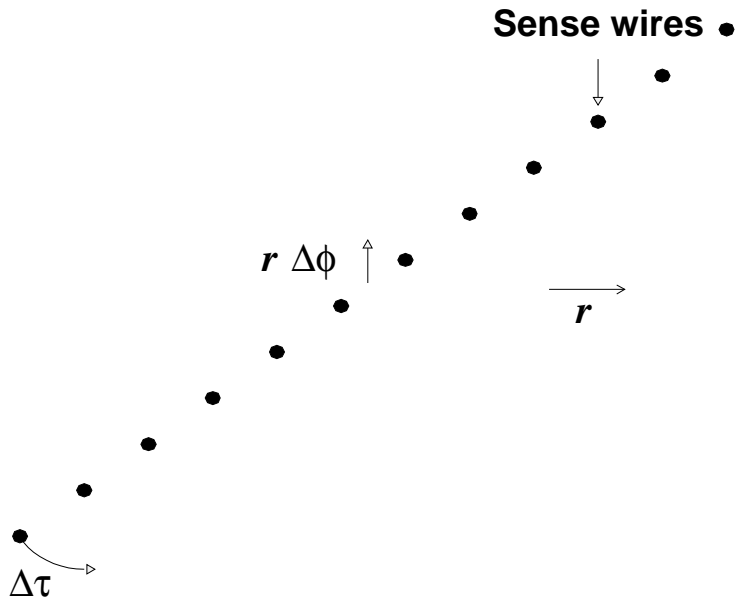


Fig. 3. A drift cell showing 12 sense wires, along with the radial (r) coordinate, and azimuthal ($r\Delta\phi$) and tilt (τ) correction parameters.

We compute the average correction to the cell tilt since the difference between the tilt corrections for the two endplates has negligible impact on tracking biases.

Finally, the functional forms describing the wire shape as a function of z , and its variation with azimuth and radius, are also tuned. These degrees of freedom are discussed in Sec. 5.

3 Cosmic ray distributions and sample selection

The cosmic ray sample used in this study is collected during collider operation by high- p_T [8] muon physics triggers, ensuring that the cosmic rays and collider tracks are recorded under the same operating conditions for the drift chamber and the spectrometer. In order to isolate a clean and unambiguous sample of cosmic rays, we require that only one or two tracks be reconstructed in the event, and that at least one of them is tagged as a muon by the presence of a matching track segment reconstructed in the muon detectors. These criteria efficiently select those cosmic-ray events which coincide in time with beam crossings in which no proton-antiproton collisions occurred. A display of such a cosmic-ray event is shown in Fig. 4. After all requirements, a sample of 207,023 cosmic-ray events is selected for the alignment study.

The spatial and temporal distributions of the cosmic rays are shown in Fig. 5.

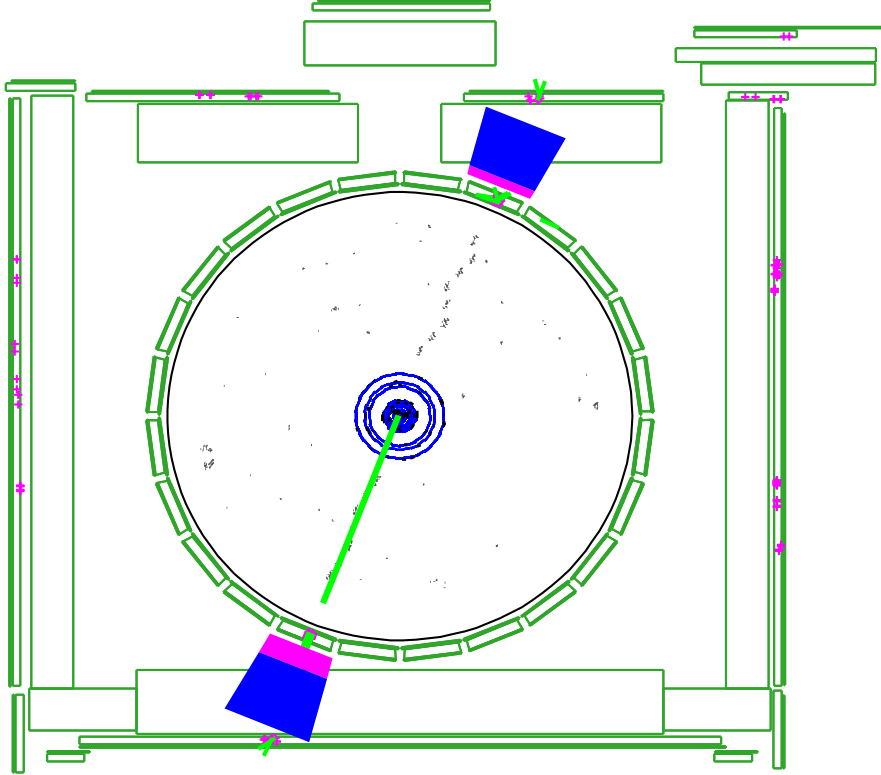


Fig. 4. Display of a cosmic-ray event recorded in coincidence with a beam crossing, in the absence of a $p\bar{p}$ collision. The reconstructed helical track trajectory shown in the bottom half of the chamber is found using the standard CDF tracking algorithm. The top half of the trajectory is found using the dedicated cosmic-ray reconstruction algorithm [3], which also combines all the hits into a single dicosmic track. The reconstructed track has $p_T \approx 69$ GeV and $\eta \approx 0.2$. The COT hits are shown at $z = 0$, resulting in a staggering of displayed hits in stereo superlayers.

The distributions of the azimuthal direction of propagation and the momentum are shown in Fig. 6.

The sample contains about 20% more positively charged than negatively charged muons, with similar momentum distributions between the two. The residuals with respect to the two-sided helical track fit (referred to as the “dicosmic track”) are an unbiased measurement of relative misalignments of the sense wires if and only if the true parameters of the cosmic ray trajectory are the same on the two sides of the COT. In this case, fitting the hits on both sides with a single helix represents a valid model of the muon’s trajectory. In practice, the muon loses on average ≈ 20 MeV of energy while passing through the silicon tracking detector. As a result, the latter half of the trajectory has lower momentum and the hit residuals will be biased with respect to the dicosmic track. Fortunately, this bias is in opposite directions for positive and negative tracks. We weight the positive and negative muons in inverse proportion to

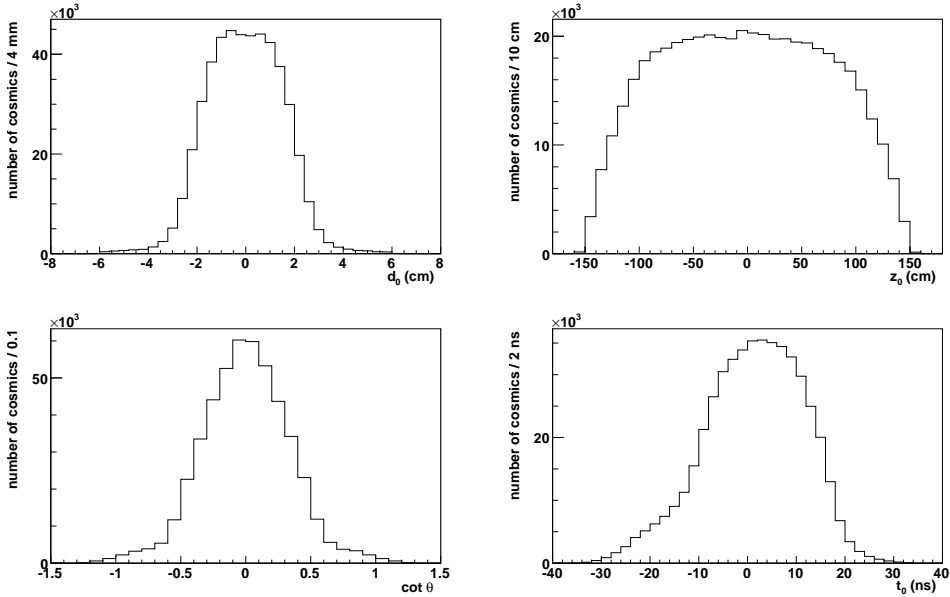


Fig. 5. Distributions of (top left) the transverse impact parameter d_0 with respect to the beam line; (top right) the longitudinal coordinate z_0 of the cosmic ray track at the point of closest approach to the beamline; (bottom left) cotangent of the polar angle; and (bottom right) the time difference t_0 between the beam crossing time and the passage of the cosmic ray. With all criteria applied except for the z_0 and hit requirements, the sample contains 484,513 cosmic-ray events.

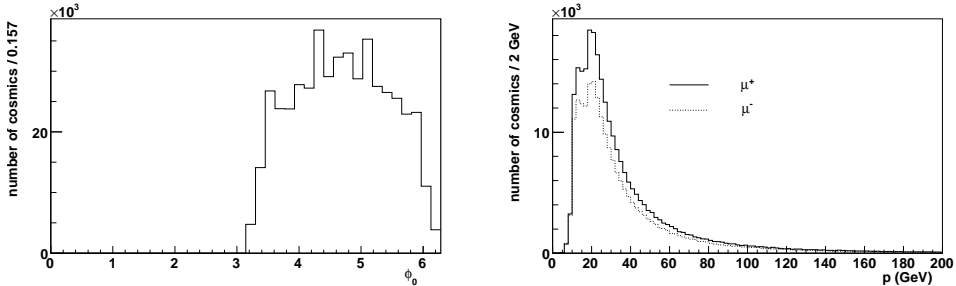


Fig. 6. Distributions of (left) the azimuthal direction of propagation ϕ_0 and (right) the momentum of the cosmic ray tracks.

their relative rates such that the average curvature (defined as q/p_T where q is the charge and p_T is the transverse momentum) of the reweighted combined sample is zero. As a result, the average residuals correspond to those of infinite-momentum tracks, and are not influenced by the energy loss.

As described in [3], the dicosmic track is seeded by a muon track found by the COT track reconstruction software which is used for collider tracks. We eliminate seed tracks with $p_T < 10$ GeV to protect against potential problems with the triggering and reconstruction of out-of-time cosmic rays. After seeding and associating hits to the dicosmic track, the dicosmic track fit [3] allows the direction of propagation and the time of incidence of the cosmic ray to be

free parameters. To ensure full containment in the COT, the dicosmic track is required to have hits in the outermost COT superlayer at both ends of its trajectory. As shown in Fig. 7, the efficiency of associating hits (from a maximum possible 192 hits) with the dicosmic track is $\approx 97\%$ for this sample. In addition to the cosmic-ray hypothesis, two additional hypotheses are also tested in the dicosmic fit: a pair of outgoing back-to-back tracks (as could be produced from a two-body decay at rest), and a pair of incoming tracks (indicating a reconstruction problem in one of the two track segments). We require the cosmic-ray hypothesis to be the χ^2 -minimizing hypothesis. The difference $\Delta\chi^2$ from the next most-likely hypothesis is an indicator of the robustness of the dicosmic track fit. The distribution of $\Delta\chi^2$, shown in Fig. 7, indicates a very strong preference for the cosmic-ray hypothesis in our selected sample. Finally, we require $|z_0| < 60$ cm to emulate the collider-track sample to which the resulting alignment constants will be applied, since CDF physics analyses make this requirement to select tracks from the longitudinal beam-crossing region.

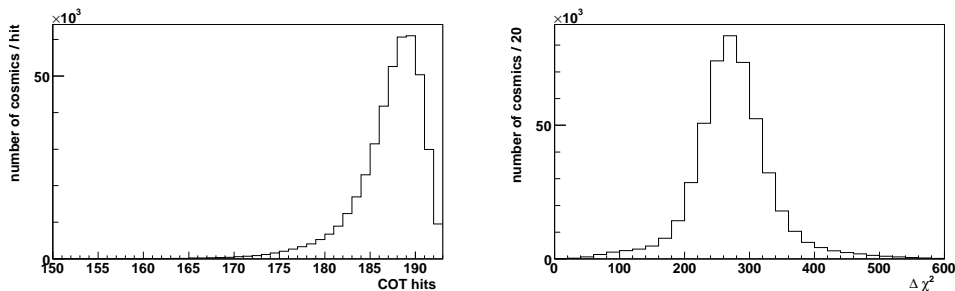


Fig. 7. Distributions of (left) the number of COT hits on the dicosmic track and (right) the difference in χ^2 between the best-fit and next-best-fit hypotheses for the directions of propagation of the two track segments.

4 Endplate alignment corrections

The starting point for obtaining the alignment correction constants is the cell-position measurements [7] made using a coordinate-measuring machine (CMM). The cell-tilt angles were updated using a calculation [9] based on a finite-element analysis (FEA) which predicted a cell-tilt correction of 1.5 mrad^2 . These measurements are used as input for the reconstruction of the cosmic-ray data. The symmetric alignment correction constants extracted from these data for each cell are shown for all superlayers in Fig. 8. The magnitude of these corrections is consistent with the nominal accuracy of the

² An independent cross-check conducted with the cosmic rays confirmed this prediction within 25%.

CMM measurements. After applying the alignment corrections iteratively, the residuals converge to zero within a statistical precision of $\approx 0.5 \mu\text{m}$, as shown in Fig. 9.

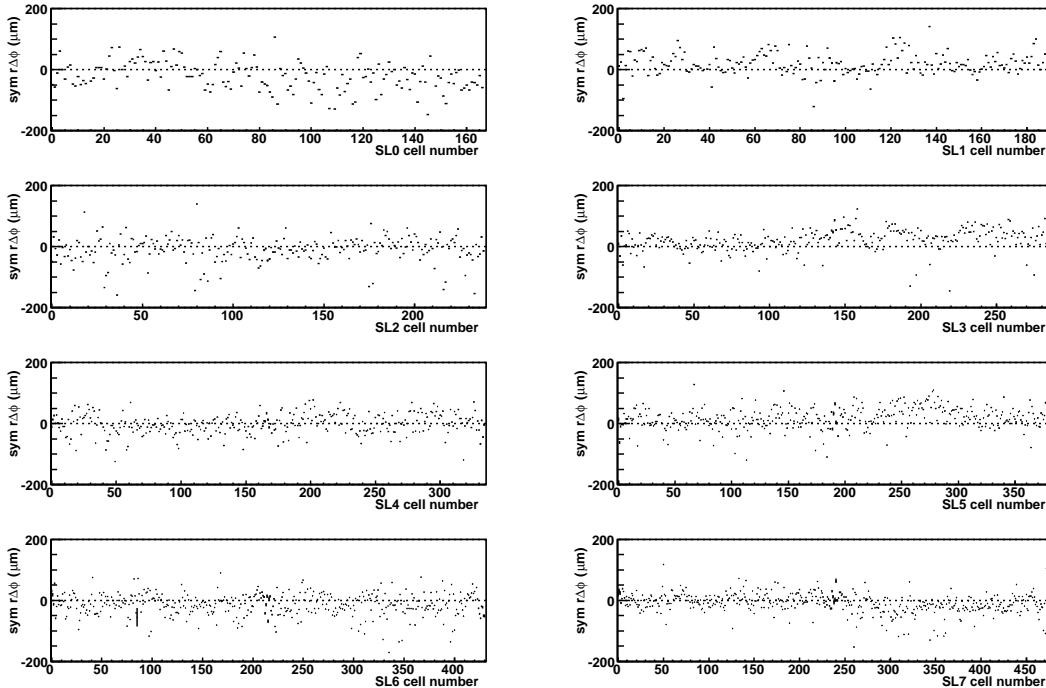


Fig. 8. Symmetric alignment corrections measured with cosmic-ray residuals, after the CMM measurements are applied in the track reconstruction. The superlayers are numbered starting from the innermost (SL0) to the outermost (SL7). The plots on the left (right) correspond to the stereo (axial) superlayers.

The asymmetric alignment correction constants extracted from the cosmic-ray data are shown for each cell in all superlayers in Fig. 10. These constants are defined as half of the difference between the east and west endplate corrections. The $|z_0| < 60 \text{ cm}$ requirement not only reduces the total cosmic-ray sample size by a factor of 2.5, but also reduces the lever-arm for measuring the z -dependence of the residuals, particularly for the superlayers at small radius. As a result, the asymmetric constants have a statistical precision of $\approx 2 \mu\text{m}$. After applying these corrections iteratively, the mean residuals shown in Fig. 11 are obtained. The convergence to zero is very good, except for a few cells that are close to the horizontal plane³ in the upper half of the stereo superlayers (labelled SL0, SL2, SL4 and SL6 respectively).

The corrections to the cell-tilt angle before applying the cosmic-ray alignment procedure are shown in Fig. 12; the residual deviations after a few iterations

³ The horizontal plane is defined by $\phi = 0$ where cells numbered zero are located. Cells numbered half of the maximum are located at $\phi = \pi$.

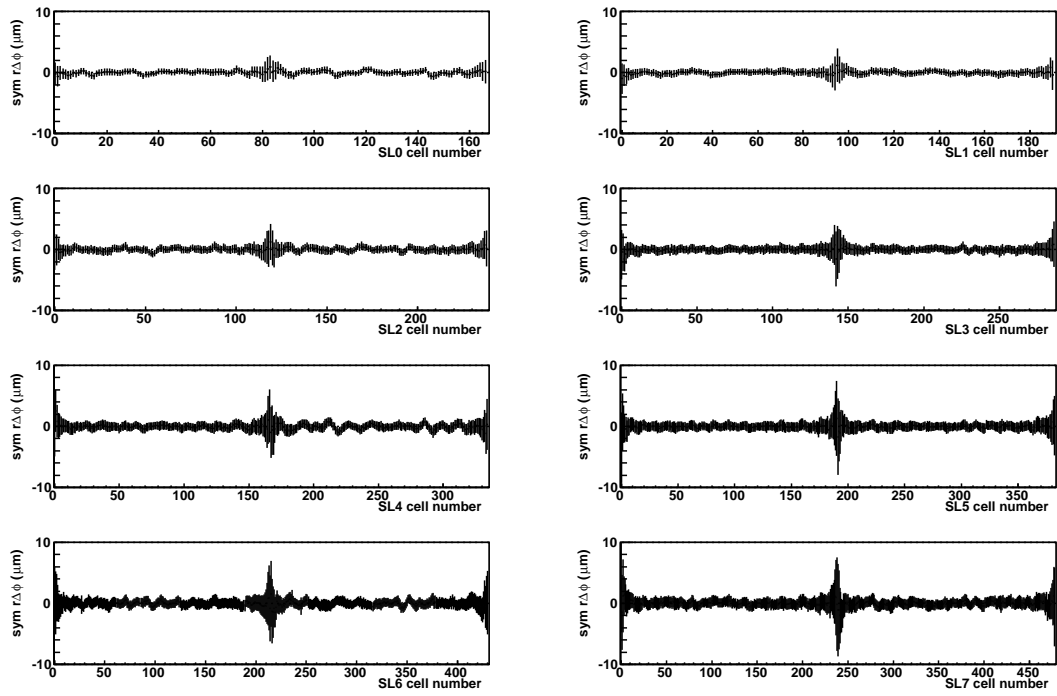


Fig. 9. Symmetric alignment constant residuals after applying the cosmic-ray corrections. Note that the vertical scale is smaller by a factor of 20 compared to Fig. 8.

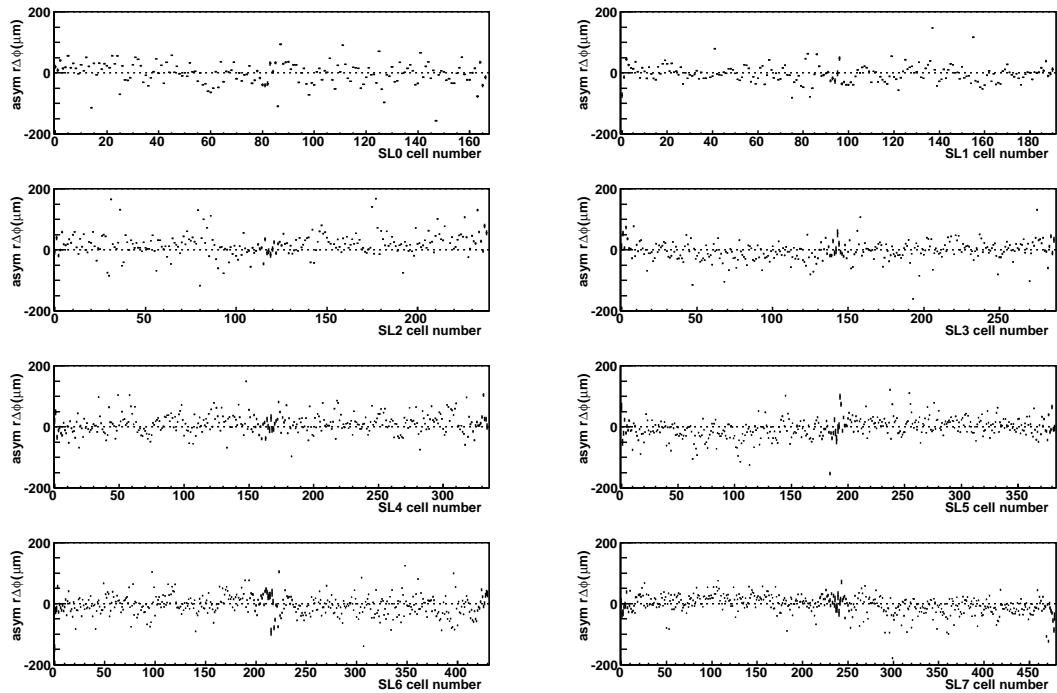


Fig. 10. Asymmetric alignment corrections measured with cosmic-ray residuals, after the CMM measurements are applied in the track reconstruction.

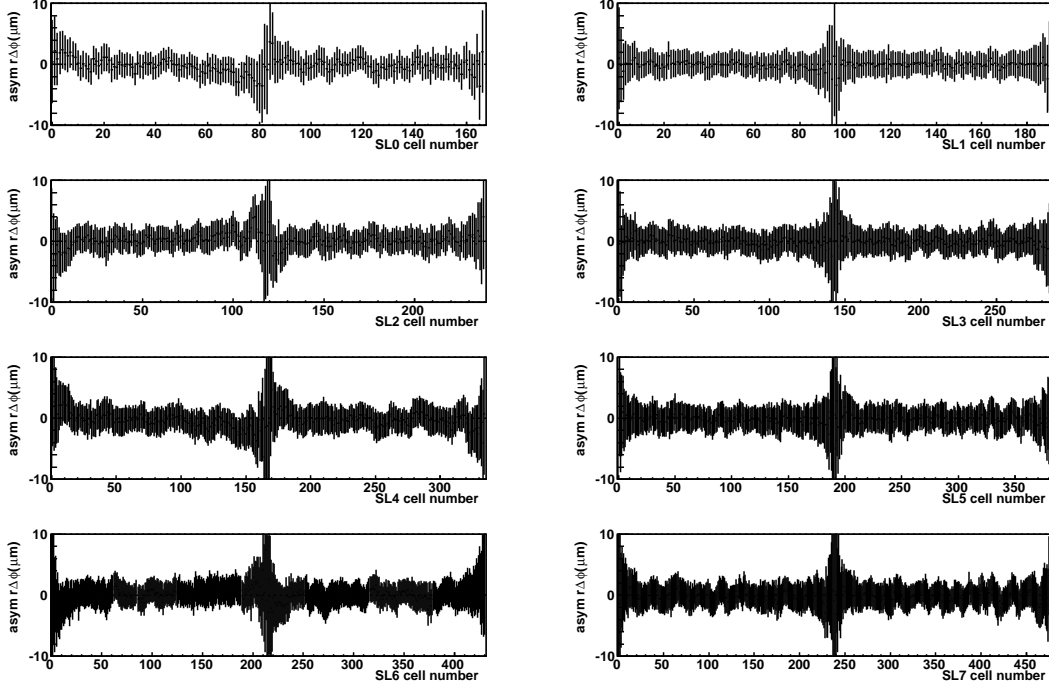


Fig. 11. Asymmetric alignment residuals after applying the cosmic-ray corrections. Note that the vertical scale is smaller by a factor of 20 compared to Fig. 10.

are shown in Fig. 13. The corrections are $\approx 500 \mu\text{rad}$ and the deviations converge to zero within a typical statistical precision of $\approx 20 \mu\text{rad}$.

5 Gravitational sag and electrostatic deflection

The corrections discussed above determine the wire positions at the endplates. The reconstructed hit coordinates also depend on the shape of the wires between the endplates. Transverse forces on the 3 m-long wires due to gravity and electrostatics cause the wires to deviate from straight lines by $O(200 \mu\text{m})$. To first order, the gravitational sag acts in the vertical direction and the electrostatic deflections occur in the direction perpendicular to the cell tilt angle (35° at $\phi = 0$). The field sheets also experience similar forces and resulting deflections. The electrostatic deflection depends on the distance of the wire from the two field sheets, coupling the deviations due to gravity and electrostatics in an azimuth-dependent way. The deflections also depend on the tension in the wires. The wire shape is modeled as a combination of a V -shape and a parabola as functions of z , to include the weight of spacers in the middle of the wires. The maximum magnitude of these functions, defined to occur at $z = 0$, is varied as a function of azimuth and radius as discussed below.

In the CDF track reconstruction, the vertical deflection (δy) of the wires with

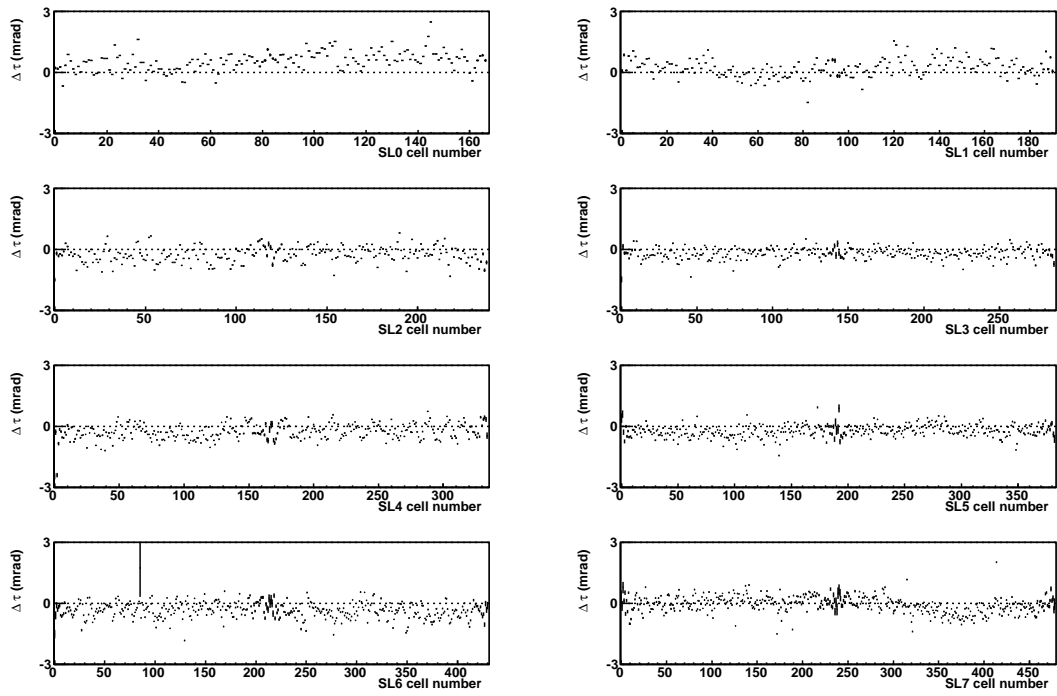


Fig. 12. Cell-tilt angle corrections measured with cosmic-ray residuals, after the CMM measurements are applied in the track reconstruction.

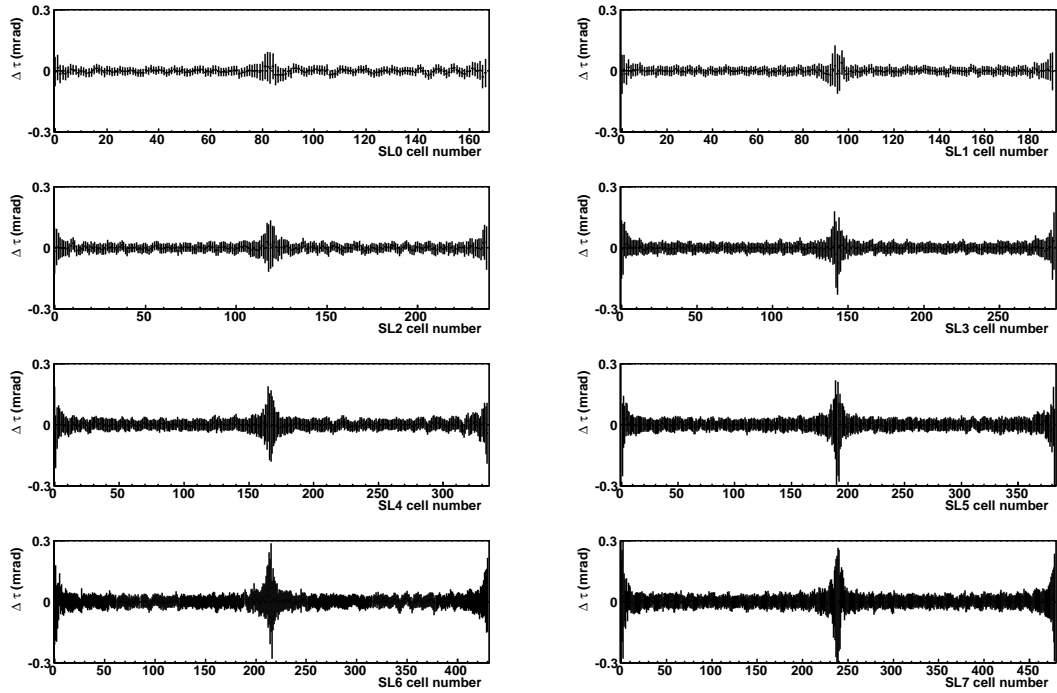


Fig. 13. Cell-tilt angle residuals after applying the cosmic-ray corrections. Note that the vertical scale is smaller by a factor of 10 compared to Fig. 12.

respect to their positions at $z = \pm 155$ cm due to gravitational sag is parameterized as follows [7]:

$$-\delta y \text{ (\mu m)} = 59(1 - |Z|) + 203(1 - Z^2) \quad (1)$$

where $Z \equiv z/(155 \text{ cm})$ and z is the longitudinal coordinate along the wire. This gravitational sag function is illustrated in Fig. 16. As discussed in [7], the coefficients were calculated using the median linear density of the wire and its nominal tension, which are expected to vary by $\pm 3\%$ and $\pm 5\%$ respectively. The first term corresponds to the center support and the second term corresponds to the weight of the wire.

The deflection due to electrostatic forces (ξ) is parameterized with the same z -dependent function but in the direction perpendicular to the sense wire plane,

$$\xi = m(\phi) [0.29(1 - |Z|) + (1 - Z^2)]. \quad (2)$$

The coefficient $0.29 = 59/203$ is the ratio of the two terms derived from Eqn. 1, such that we use the same wire shape as a function of z for describing both gravitational sag and electrostatic deflection. The magnitude modulation function $m(\phi)$ is measured [7] to vary sinusoidally with the azimuthal orientation ϕ_{wp} of the wire plane,

$$m(\phi) = a \cos \phi_{\text{wp}} + o \quad (3)$$

where the azimuthal dependence arises from the different gravitational sags of the sense wires and the field sheets. The sign and phase convention is such that the electrostatic deflection of the sense wire plane is upwards (opposite the gravitational sag) when the sense wire plane is horizontal. The amplitude $a = 117 \text{ }\mu\text{m}$ and the offset $o = -84 \text{ }\mu\text{m}$ were measured in a preproduction prototype with an electric field of 2.4 kV/cm , and scaled down by a factor of 2.7 to account for the COT operating point of 1.9 kV/cm [7], such that $a = 43 \text{ }\mu\text{m}$ and $o = -31 \text{ }\mu\text{m}$ are applied to the collider data.

The alignment corrections and the wire-shape functions can be cross-checked by comparing the track parameters of the two segments of the cosmic ray track. The sum or difference (depending on the definition of the track parameter) of the track parameters, defined at the point of closest approach to the beamline, should be consistent with zero within resolution. The convention for computing the pull for ϕ_0 , z_0 and t_0 is that the outgoing segment is positive and incoming segment is negative. In the case of curvature, d_0 and $\cot \theta$, the pull is defined as the sum of the two segments' parameters, since the sign changes from top to bottom.

Our studies of the track-parameter pulls in the cosmic-ray data show significant dependence on $\cot\theta$ after the above wire-shape functions are applied, as shown in Fig. 14. In particular, the mean pulls for the curvature, impact parameter and $\cot\theta$ show a large quadratic dependence on $\cot\theta$. We find

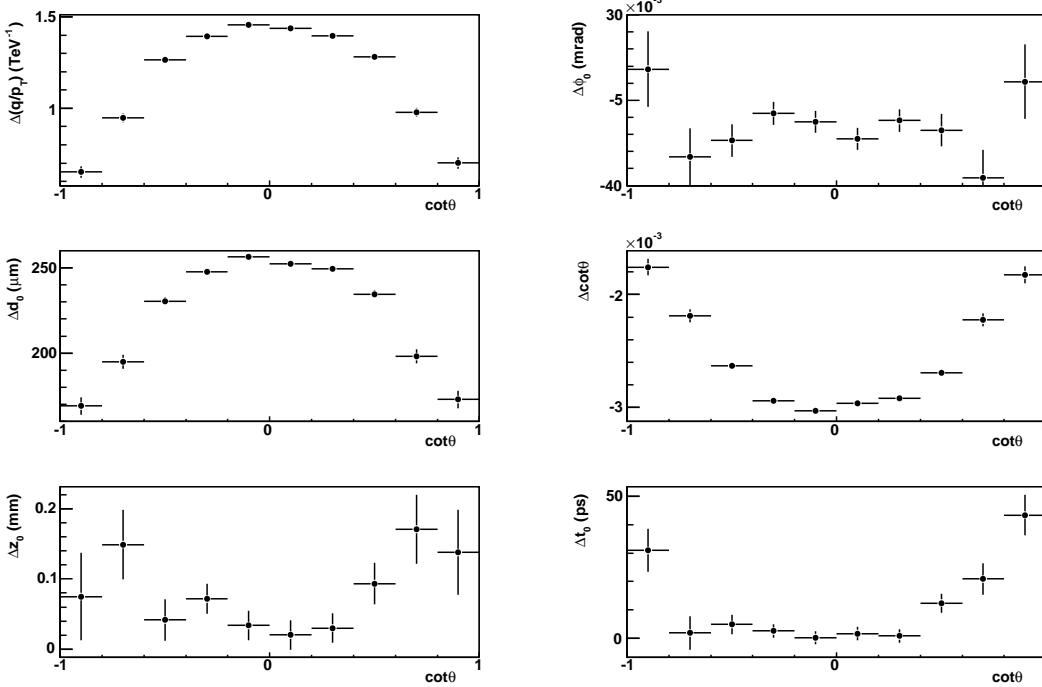


Fig. 14. Track parameter pulls as a function of $\cot\theta$ after the cosmic-ray alignment corrections and the default wire-shape functions are applied in the track reconstruction.

that these variations of the pulls can be reduced by incorporating a radius-dependent magnitude modulation function $m(\phi) \rightarrow m(R, \phi)$, as follows,

$$m(R, \phi) = a(R) \cos \phi_{\text{wp}} + o(R), \quad (4)$$

where $R \equiv r/(140 \text{ cm})$ and r is the radial position of the wire. We use the pull measurements from the cosmic-ray data to tune the radius-dependent offset function, $o(R) = o + \delta o(R)$, where

$$\delta o(R) = b_0 + b_1 R + b_2 R^2. \quad (5)$$

The coefficients b_i account for the inward bending of the endplates as a function of radius (see Fig. 10 of [7]) and the possible effect on the wire tension, resulting in radius-dependent corrections to the electrostatic deflection. The stereo superlayers experience additional electrostatic effects due to the twisting forces induced by the stereo angle [7]. Therefore, we tune the coefficients in Eqn. 5 separately for the axial and stereo superlayers in order to minimize

the remaining biases, with the resulting values shown in Table 1. A small correction to the sinusoidal amplitude $a(R)$ is also introduced to reduce pull biases as a function of ϕ_0 :

$$a(R) = a \left[1 + 0.03 \frac{\delta o(R)}{o} \right] , \quad (6)$$

resulting in $a(R)$ varying between $45 \mu\text{m}$ and $49 \mu\text{m}$ for the different superlayers. The values of $o(R)$ and $a(R)$ that we use are shown in Table 2. The values of $o(R)$ are modified substantially compared to the nominal value of $-31 \mu\text{m}$, justifying the inclusion of the additional degrees of freedom in Eqn. 5. The radial dependence of the wire shapes deduced from the cosmic-ray data is illustrated in Fig. 15.

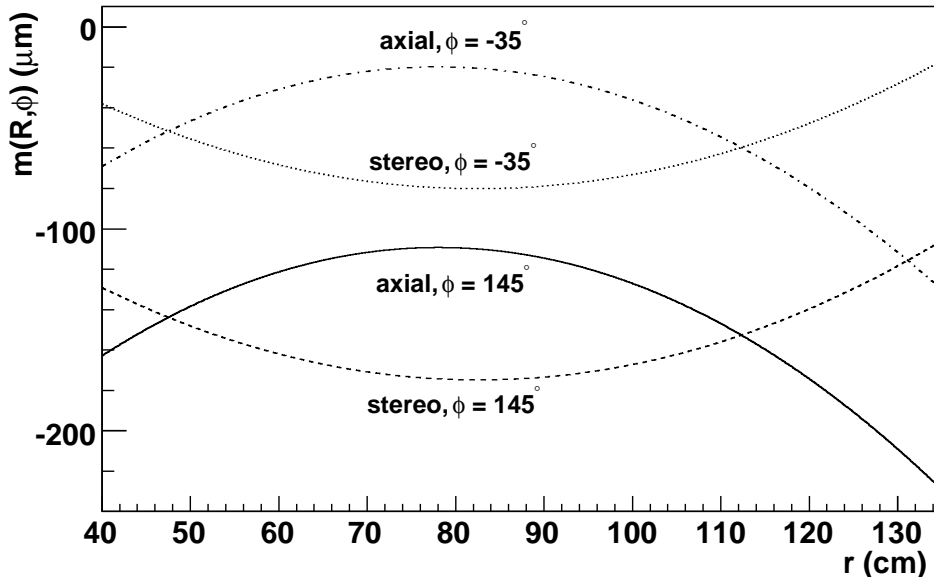


Fig. 15. The radius-dependent electrostatic deflection at $z = 0$, for axial and stereo superlayers. The sinusoidal dependence on azimuth is bounded by the curves shown for $\phi = -35^\circ$ and $\phi = 145^\circ$ respectively, where $\cos \phi_{\text{wp}} = \pm 1$ in Eqn. 4.

The replacement of $m(\phi)$ by $m(R, \phi)$ substantially reduces the dependence of the pulls on $\cot \theta$, z_0 , and ϕ_0 , as shown in Sec. 7.

6 Drift model

The wire positions are transferred to hit positions by the drift model, which converts the drift-time measurement to a hit distance from the wire. The local

	b_0	b_1	b_2
axial superlayers	-250	777	-696
stereo superlayers	68	-558	473

Table 1

Parameters in the wire-shape functions described in Eqn. 5, in units of μm .

superlayer	$a(R)$ (μm)	$o(R)$ (μm)
SL0	46	-96
SL1	45	-78
SL2	47	-124
SL3	45	-65
SL4	47	-124
SL5	46	-91
SL6	46	-98
SL7	49	-157

Table 2

Parameters describing the electrostatic deflection varying with azimuth as given by Eqn. 4.

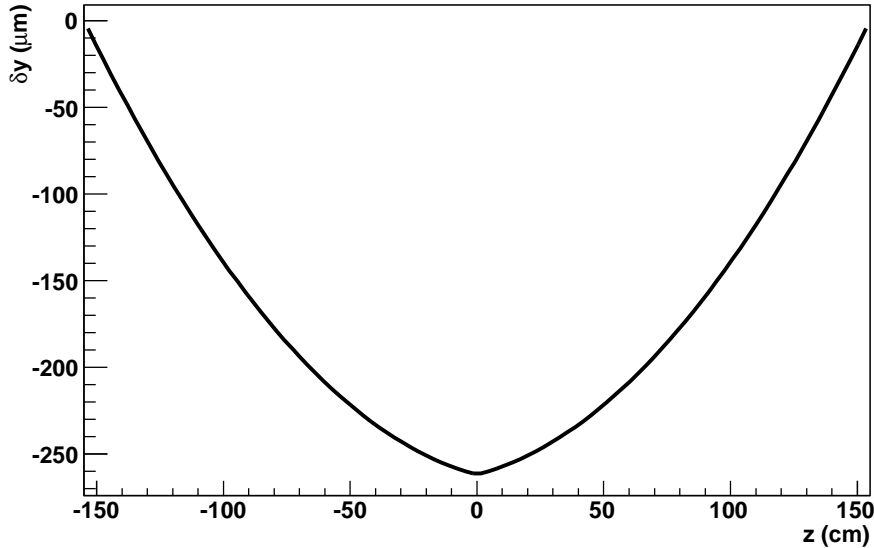


Fig. 16. The gravitational sag of the wires (Eqn. 1) as a function of z . The same z -dependence, normalized by the magnitude modulation function $m(R, \phi)$ (Eqns. 2 and 4) also describes the electrostatic deflection perpendicular to the sense wire plane.

coordinate is denoted by Y (where the sign denotes whether the coordinate is on the left or right side of the sense wire in the cell) and the local distance is denoted by $D \equiv |Y|$. The residual $\Delta Y \equiv Y_{\text{hit}} - Y_{\text{track}}$ is used for the alignment results discussed above. The residual $\Delta D \equiv \text{sign}(Y_{\text{track}}) \times \Delta Y$, is used to study the drift model. The simplest drift model would be parameterized by a timing offset (due to propagation delays in the electronic read-out path) and a drift speed, if the time-distance relationship were proportional. In practice, this simple drift model describes the time-distance relationship well in the $\approx 2\text{-}7$ mm range of drift distance. The regions close to the wire and the field sheets require additional parameters to describe the non-linear time-distance relationships in those regions. An elaborate drift model has been developed and is used in the CDF track reconstruction [7].

For the cosmic-ray-based alignment study discussed here, we perform additional tuning of this drift model, particularly in the non-linear regions, by iteratively reducing the dependence of ΔD on Y_{track} . The final results for each superlayer are shown in Fig. 17. In addition to tuning the drift model parameters, we also tune the timing offset for each cell so that $\langle \Delta D \rangle = 0$ over all hits in the cell. The differences in timing offsets for different wires within a cell, as well as their variation with time, have been separately calibrated by an electronic calibration pulse injection system [7]. As Fig. 17 shows, the residuals ΔD are typically less than $10 \mu\text{m}$ over most of the drift region. The remaining mismodeling in the nearest and farthest ≈ 1 mm region from the wires, of about $20 \mu\text{m}$, is small compared to the hit resolution of $\approx 140 \mu\text{m}$.

7 Cross-checks of track parameter biases

The distributions of the pulls are shown in Fig. 18 using the CMM measurements and in Fig. 19 after the cosmic-ray-based alignment corrections and our wire-shape tunes are applied. The average values are consistent with zero, and the resolution is improved by $\approx 25\%$, after the alignment.

Overlays of the pulls before and after the cosmic-ray alignment are shown in Fig. 20-25.

The pulls as a function of azimuth (Fig. 20) show substantial variation before alignment. The variation is largely eliminated by the alignment, as shown again in Fig. 21 on a finer scale. The pulls as a function of z_0 are also substantially improved by the alignment, as can be seen in Fig. 22. The final pulls are shown in Fig. 23 on a finer scale. Similar improvement is seen in the variation of the pulls as a function of polar angle, in the comparison shown in Fig. 24. A close-up view of these pulls after the alignment is shown in Fig. 25.

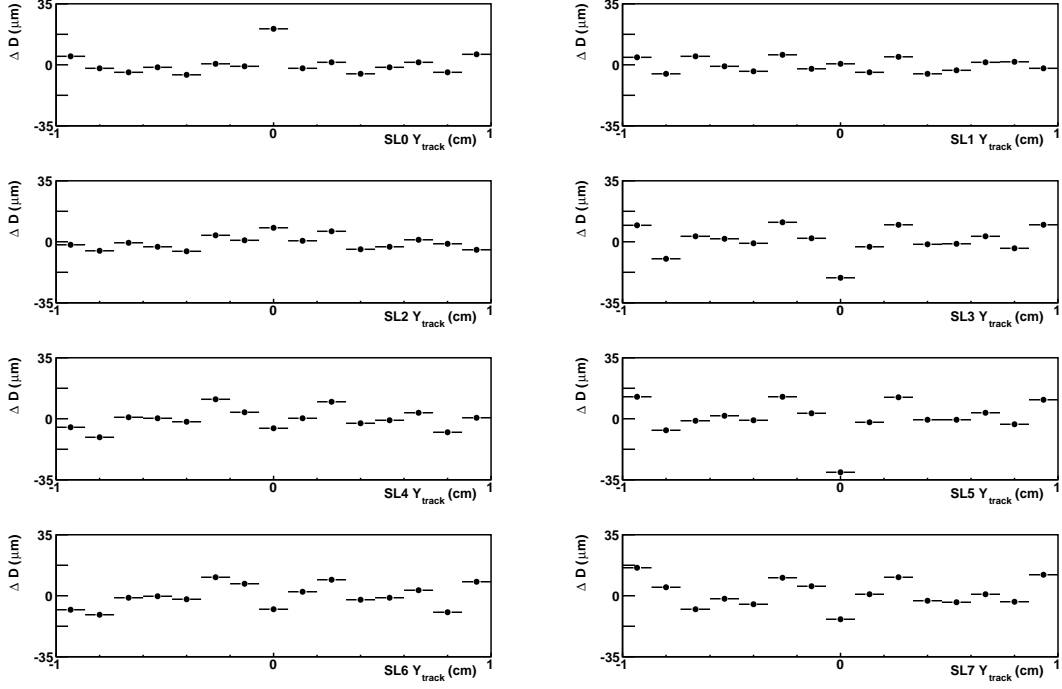


Fig. 17. The mean ΔD as a function of local track coordinate Y_{track} in the cell for the eight superlayers.

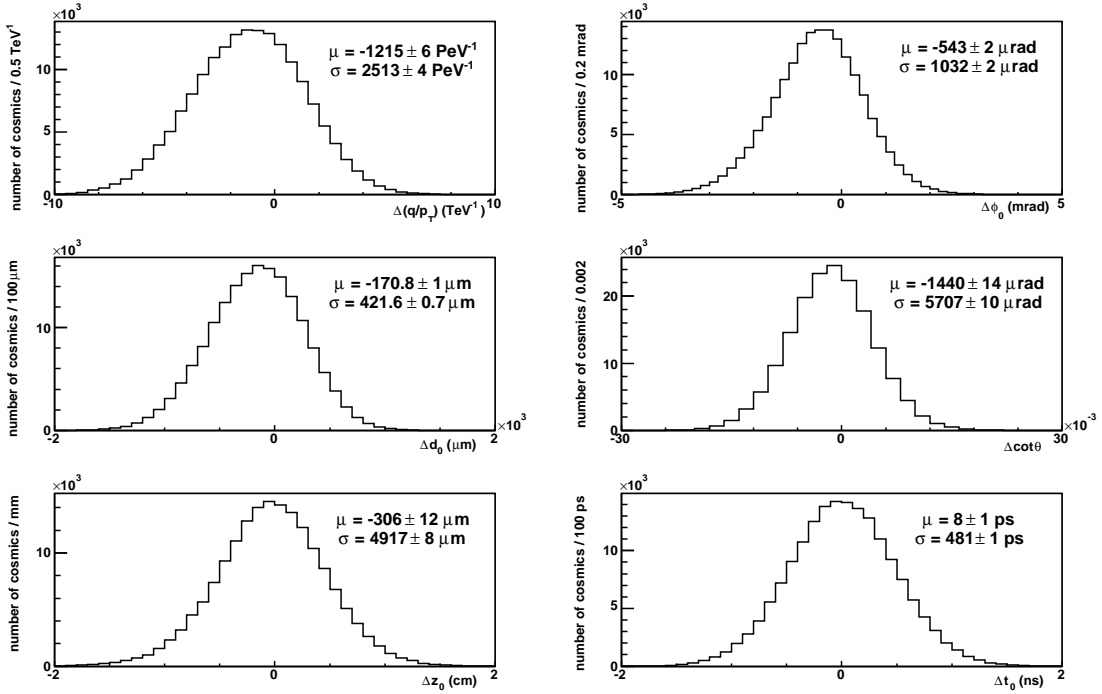


Fig. 18. Track parameter pulls after the CMM measurements are applied in the track reconstruction, shown with the mean (μ) and standard deviation (σ).

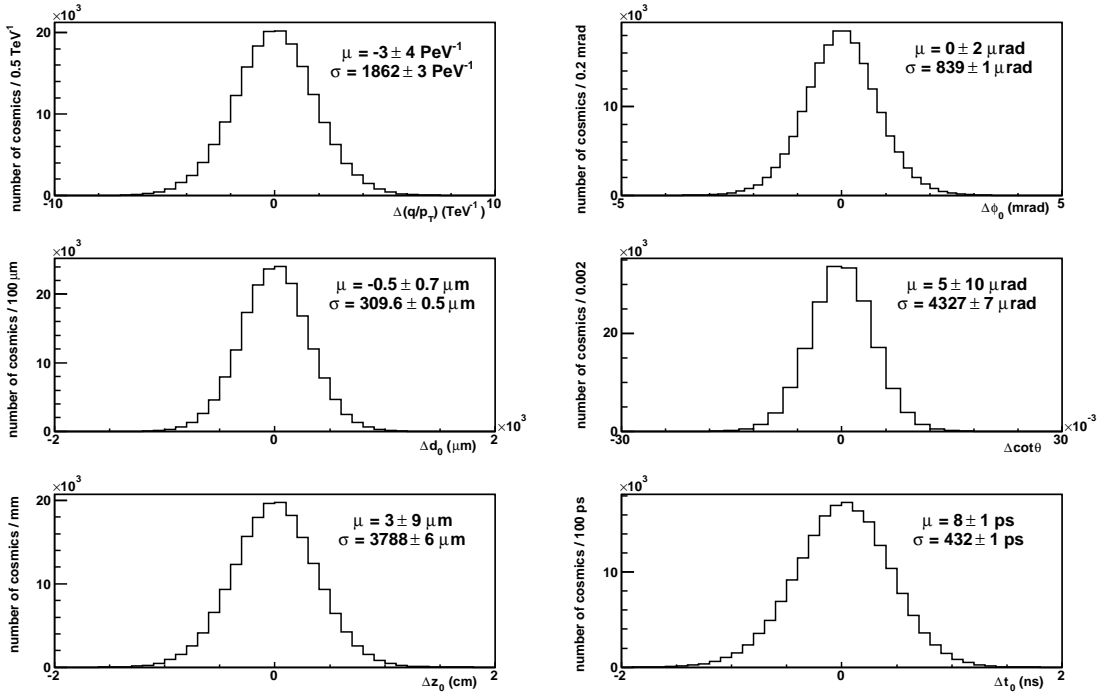


Fig. 19. Track parameter pulls after applying the cosmic-ray corrections, shown with the mean (μ) and standard deviation (σ).

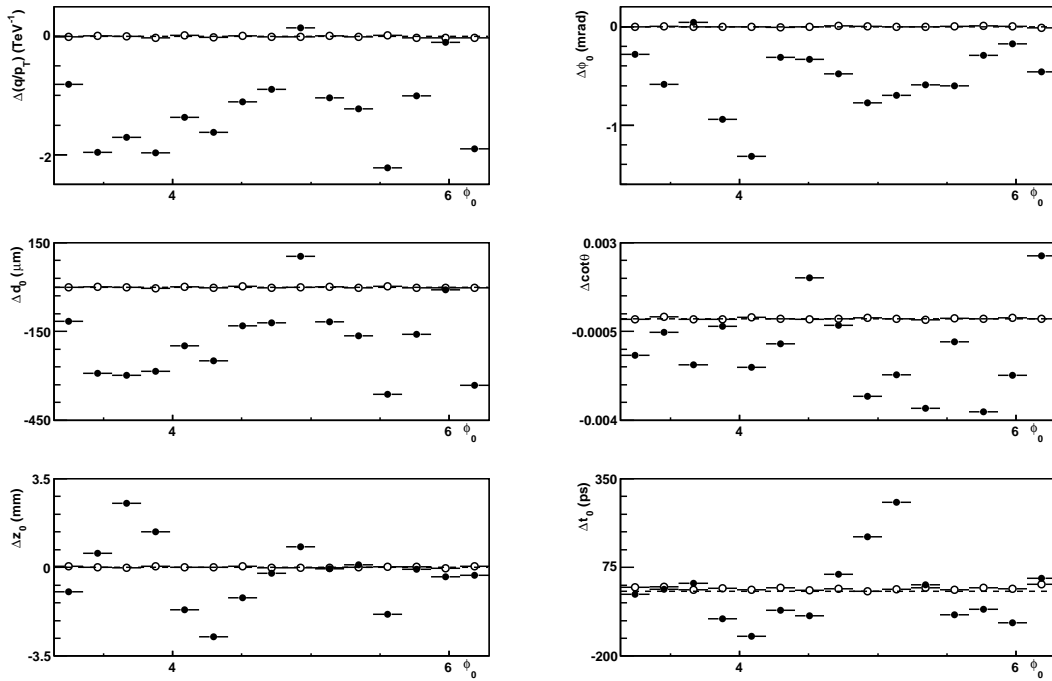


Fig. 20. Track parameter pulls as functions of ϕ_0 before (solid circles) and after (open circles) the cosmic-ray alignment.

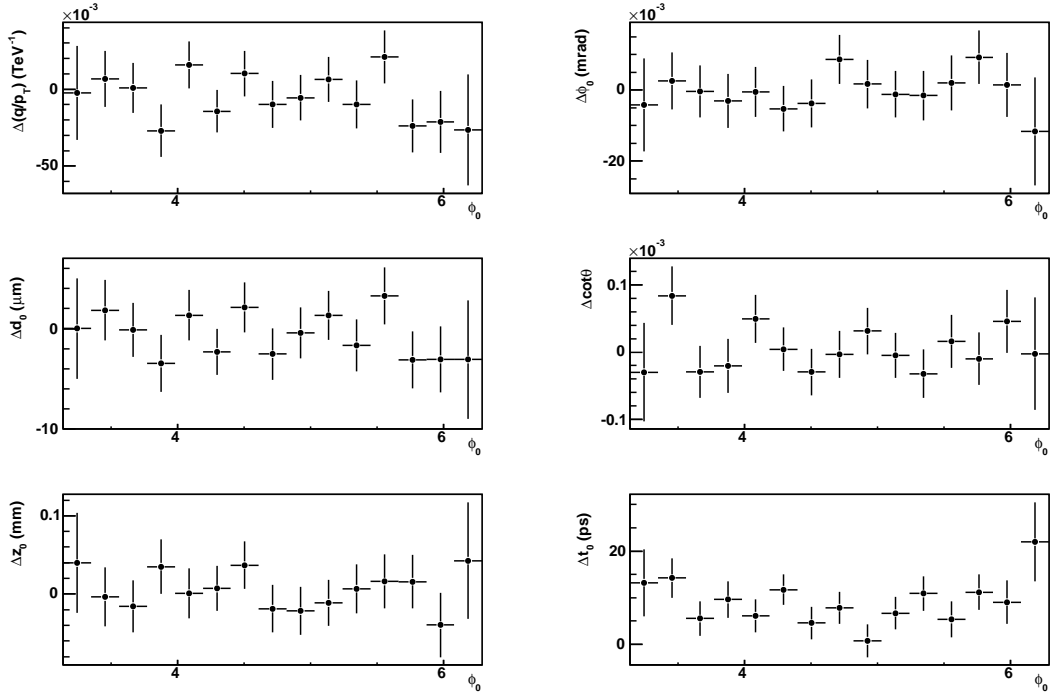


Fig. 21. Track parameter pulls as functions of ϕ_0 after applying the cosmic-ray corrections.

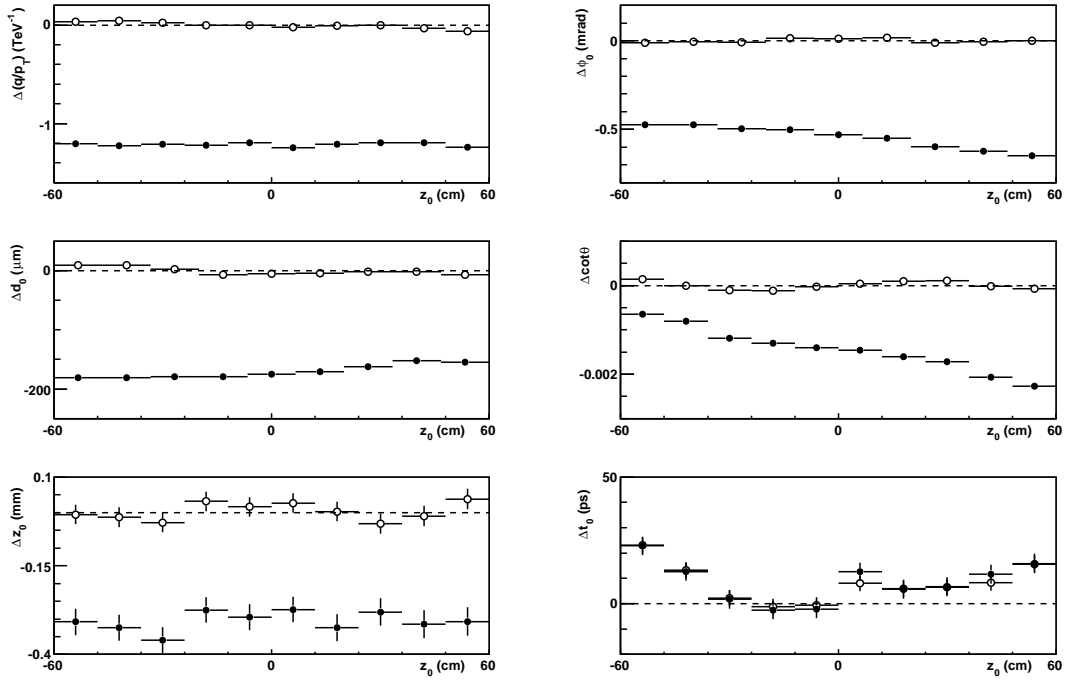


Fig. 22. Track parameter pulls as functions of z_0 before (solid circles) and after (open circles) the cosmic-ray alignment.

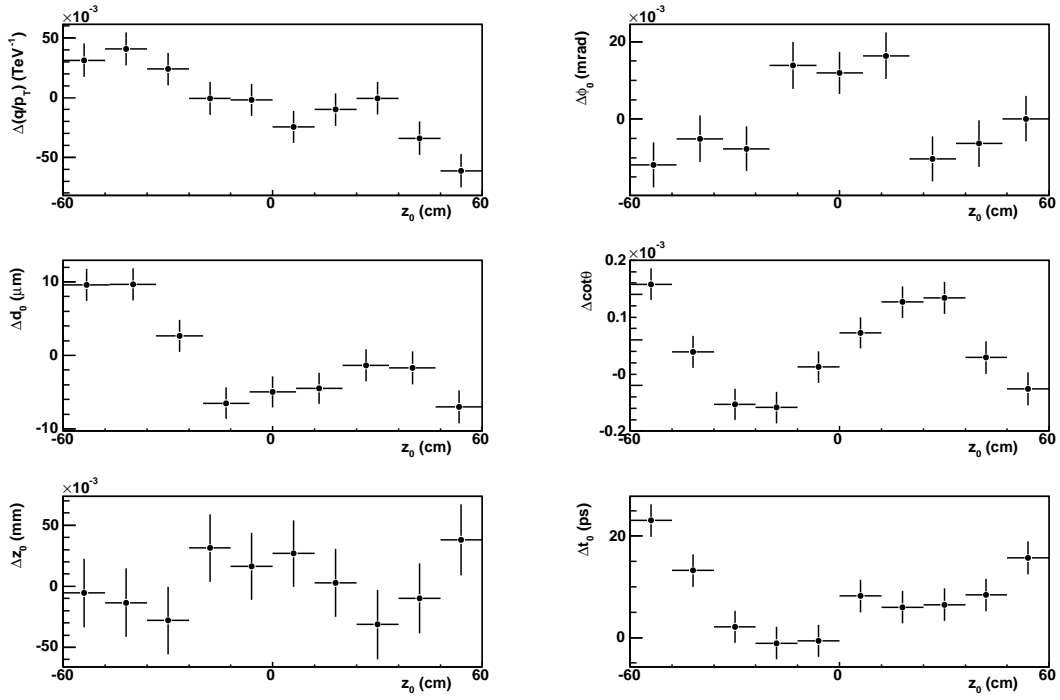


Fig. 23. Track parameter pulls as functions of z_0 after applying the cosmic-ray corrections.

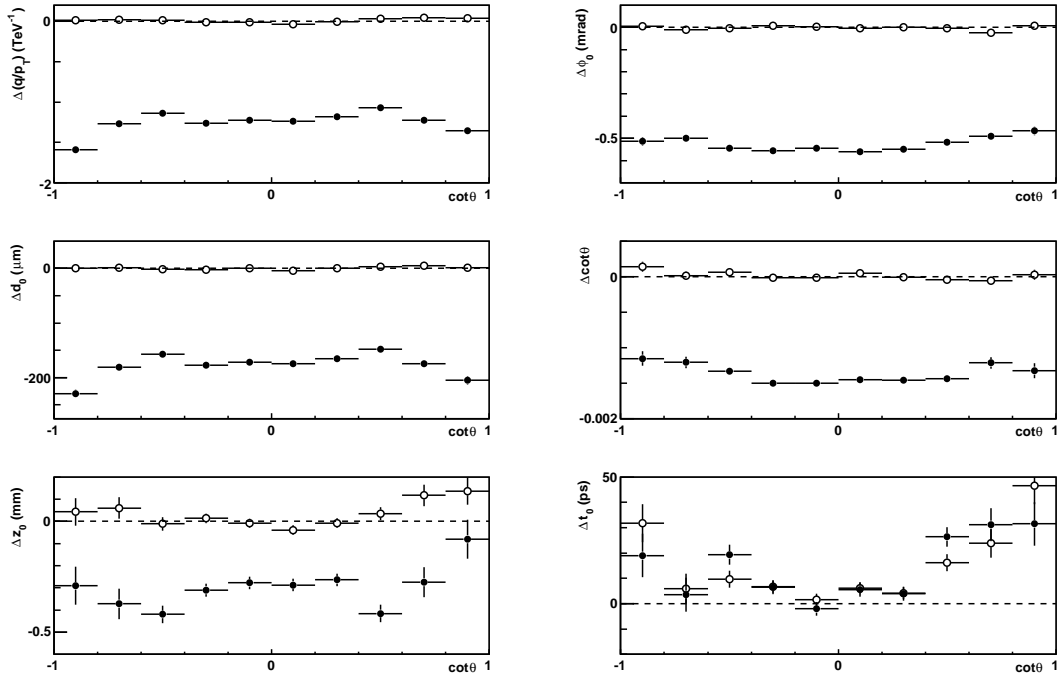


Fig. 24. Track parameter pulls as functions of $\cot\theta$ before (solid circles) and after (open circles) the cosmic-ray alignment.

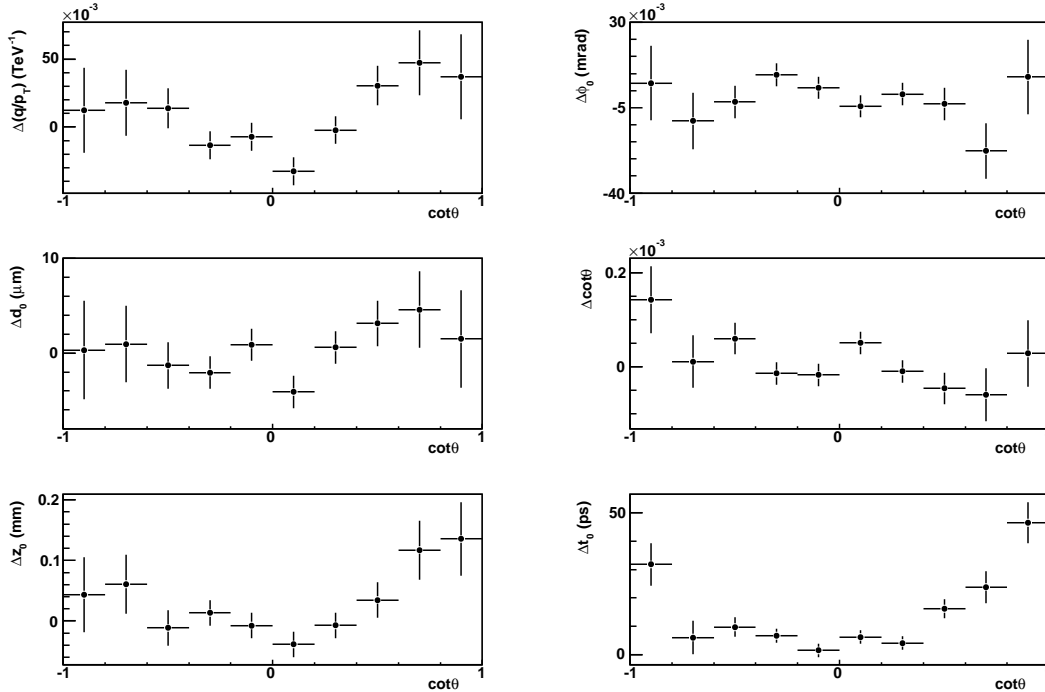


Fig. 25. Track parameter pulls as functions of $\cot \theta$ after applying the cosmic-ray corrections.

8 Conclusions

The precise alignment of the CDF drift chamber, which provides the basis of the track momentum calibration for the measurement of the W boson mass, is performed using a sample of cosmic rays collected *in situ* with the collider data. Special reconstruction and track fitting algorithms are employed to associate and fit the hits on both sides of the drift chamber with a single helical trajectory. The hit residuals with respect to this reference track provide information on the relative alignment of the drift chamber cells, and on the coherent deformations of the drift chamber. Relative rotations of the radial superlayers and relative twists of the endplates are well-constrained by our procedure while, in particular, these modes of deformation are not well-constrained by residuals with respect to tracks from $p\bar{p}$ collisions.

We align the wires to sub-micron statistical precision, and constrain the differences between the endplates to the precision of a few microns. We have also tuned the wire-shape functions describing the deflections due to electrostatic forces to a similar precision. The drift model, and in particular the non-linear time-to-distance relations close to the wire and field sheet, has been updated.

Remaining biases on track parameters are, on average, sub-micron on the impact parameter and $< 1\%$ on the curvature of a $p_T = 1$ TeV particle; the variations with z_0 , ϕ_0 and $\cot \theta$ are within a factor of five of the average bias.

Acknowledgements

We wish to thank our colleagues on the CDF experiment at the Fermi National Accelerator Laboratory. We thank Aseet Mukherjee, Robert Wagner and Oliver Stelzer-Chilton for useful discussions, and Yu Zeng for his help in isolating the cosmic-ray data. We acknowledge the support of the U.S. Department of Energy and the Science and Technology Facilities Council of the United Kingdom.

References

- [1] CDF Collaboration (T. Aaltonen *et al.*), Phys. Rev. Lett. **99**, 151801 (2007); *ibid.*, Phys. Rev. D **77**, 112001 (2008).
- [2] CDF Collaboration (T. Aaltonen *et al.*), Phys. Rev. Lett. **108**, 151803 (2012); *ibid.*, Phys. Rev. D **89**, 072003 (2014).
- [3] A. V. Kotwal, H. K. Gerberich, and C. Hays, Nucl. Instrum. Methods Phys. Res. A **506**, 110 (2003).
- [4] CDF Collaboration (F. Abe *et al.*), Nucl. Instrum. Meth. **A271**, 387 (1988).
- [5] CDF Collaboration (D. Acosta *et al.*), Phys. Rev. D **71**, 032001 (2005).
- [6] CDF Collaboration (A. Abulencia *et al.*), J. Phys. G: Nucl. Part. Phys. **34**, 2457 (2007).
- [7] T. Affolder *et al.*, Nucl. Instrum. Meth. **A 526**, 249 (2004).
- [8] Pseudorapidity is defined as $\eta = -\ln[\tan(\theta/2)]$, where θ is the polar angle from the beam axis. The azimuthal angle is denoted by ϕ . Energy (momentum) transverse to the beam is denoted as E_T (p_T). We use the convention $c = 1$ throughout this paper.
- [9] Aseet Mukherjee and Robert L. Wagner, private communication.